

A&A 530, A125 (2011)
DOI: [10.1051/0004-6361/201016198](https://doi.org/10.1051/0004-6361/201016198)
© ESO 2011

A comprehensive approach to analyzing the *XMM-Newton* data of Seyfert 1 galaxies

M. V. Cardaci^{1,2,3}, M. Santos-Lleó², G. F. Hägele^{1,3,*}, Y. Krongold⁴, A. I. Díaz¹, and P. Rodríguez-Pascual²

¹ Universidad Autónoma de Madrid, Ctra. de Colmenar Km.15, Cantoblanco, 28049 Madrid, Spain
e-mail: monica.cardaci@uam.es

² XMM-Newton Science Operations Center, ESAC, ESA, POB 78, 28691 Villanueva de la Cañada, Madrid, Spain

³ Facultad de Cs. Astronómicas y Geofísicas, Universidad Nacional de La Plata, Paseo del Bosque s/n, 1900 La Plata, Argentina

⁴ Instituto de Astronomía, Universidad Nacional Autónoma de México, Apartado Postal 70-264, 04510 México DF, México

Received 24 November 2010 / Accepted 15 March 2011

ABSTRACT

Aims. We seek a comprehensive analysis of all the information provided by the *XMM-Newton* satellite of the four Seyfert 1 galaxies ESO 359-G19, HE 1143-1810, CTS A08.12, and Mrk 110, including the UV range, to characterize the different components that are emitting and absorbing radiation in the vicinity of the active nucleus.

Methods. The continuum emission was studied through the EPIC spectra by taking advantage of the spectral range of these cameras. The high-resolution RGS spectra were analyzed to characterize the absorbing and emission line features that arise in the spectra of the sources. All these data, complemented by information in the UV, are analyzed jointly in order to achieve a consistent characterization of the observed features in each object.

Results. The continuum emission of the sources can be characterized either by a combination of a power law and a black body for the weakest objects or by two power law components for the brightest ones. The continuum is not absorbed by neutral or ionized material in the line of sight to any of these sources. In all of them we have identified a narrow Fe-K α line at 6.4 keV. In ESO 359-G19 we also find an FeXXVI line at about 7 keV. In the soft X-rays band, we identify only one O VII line in the spectra of HE 1143-1810 and CTS A08.12, and two O VII-He α triplets and a narrow O VIII-Ly α emission line in Mrk 110.

Conclusions. Not detecting warm material in the line of sight to the low state objects is due to intrinsically weaker or absent absorption in the line of sight and not to a low signal-to-noise ratio in the data. Besides this, the absence of clear emission lines cannot be fully attributed to dilution of those lines by a strong continuum.

Key words. galaxies: active – galaxies: Seyfert – galaxies: general – X-rays: galaxies

1. Introduction

The spectral features characteristic of the X-ray spectra of active galactic nuclei (AGNs) are conspicuous signatures of the physical processes taking place in the inner regions of these objects, and analyzing them has significantly improved our understanding of these issues in the last few years of the 20th century. However, it has also become evident that a much better understanding is needed, and in fact it can be achieved by detailed analysis of the data acquired with the present generation of X-ray telescopes.

In this paper we present a comprehensive analysis of all the available data obtained with the *XMM-Newton* satellite of four Seyfert 1 galaxies: ESO 359-G19, HE 1143-1810, CTS A08.12, and Mrk 110 in order to try to characterize the different components of the gas that imprint the absorption and emission features in the X-ray spectra of these objects. The low-resolution and large spectral range EPIC (European Photon Image Camera) spectra were used to study the continuum emission. The high-resolution RGS (Reflection Grating Spectrometer) spectra are analyzed to search for and characterize, if found, the absorbing and emission line features that arise in the spectra of these sources.

The first of our objects, ESO 359-G19, has been classified as a Seyfert 1 galaxy by [Maza et al. \(1992\)](#) using longslit

spectrophotometric data. It has not been studied in detail in spite of being observed on many occasions ([Fairall 1988](#); [Wisotzki et al. 1996](#); [Karachentsev & Makarov 1996](#)). It was previously observed in X-rays with the ROSAT (1990 August; [Voges et al. 1999](#); [Thomas et al. 1998](#)) and *Einstein* ([Elvis et al. 1992](#)) satellites, as part of the study of the general properties of objects with X-ray emission ([Simcoe et al. 1997](#); [Grupe et al. 2001](#); [Jahnke & Wisotzki 2003](#); [Fuhrmeister & Schmitt 2003](#)). More recently, it has been observed by Swift (2008 October) as part of a sample of 92 bright soft X-ray selected AGNs ([Grupe et al. 2010](#)).

HE 1143-1810 was classified as a type 1 Seyfert AGN by [Remillard et al. \(1986\)](#). These authors also found that this galaxy has a companion object, LEDA 867889, which shows neither signatures of nuclear activity nor the characteristic emission of H II galaxies. It is located at about 20 kpc from HE 1143-1810. From extreme UV observations with FUSE, [Wakker et al. \(2003\)](#) studied the gas surrounding the AGN and concluded that the positive-velocity O VI absorption extends much further than expected for a Galactic origin, although they did not find a clear separation between an intrinsic O VI line and the Galactic absorption. The authors separated the thick disk and high-velocity cloud components at a velocity of 100 km s⁻¹. However, using the same and newer observations from FUSE, [Dunn et al. \(2007\)](#) could not identify any intrinsic absorption feature in this galaxy.

Very little is known in detail about CTS A08.12, despite its being included in a large number of statistical studies at different

* CONICET, Argentina.

Table 1. General characteristics of the objects selected for our study.

Object	α_{2000}	δ_{2000}	z	Distance (Mpc)*	N_{H} (cm^{-2})
ESO 359-G19	04 ^h 05 ^m 01.7 ^s	-37° 11' 15" 0	0.056 ^(a)	224	1.02×10^{20}
HE 1143-1810	11 ^h 45 ^m 40.5 ^s	-18° 27' 16" 0	0.033 ^(b)	132	3.40×10^{20}
CTS A08.12	21 ^h 32 ^m 02.2 ^s	-33° 42' 54" 0	0.029 ^(c)	116	4.07×10^{20}
Mrk 110	09 ^h 25 ^m 12.9 ^s	+52° 17' 11" 0	0.035 ^(d)	140	1.42×10^{20}

Notes. * From the object redshifts using the expression $D = (cz/H_0)$ and adopting $H_0 = 75 \text{ km s}^{-1} \text{ Mpc}^{-1}$. Estimated hydrogen column densities from Dickey & Lockman (1990).

References. ^(a) Reimers et al. (1996), ^(b) da Costa et al. (1998), ^(c) Rodríguez-Ardila et al. (2000), ^(d) Boroson & Green (1992).

wavelengths (e.g. Voges et al. 1999; Bauer et al. 2000; Ebisawa et al. 2003; Verrecchia et al. 2007; Mauch & Sadler 2007). It was classified as a Seyfert 1 by Maza et al. (1994).

Finally, Mrk 110 is a nearby Seyfert 1 galaxy with a very irregular morphology (Bischoff & Kollatschny 1999), which may indicate that it has suffered some kind of interaction with a companion galaxy (Hutchings & Craven 1988). From optical spectroscopy covering a narrow spectral range, between 4300 and 5700 Å, Boroson & Green (1992) estimated a full width at half maximum (*FWHM*) of 2120 km s^{-1} for the H β emission line, and observed a very broad He I 4471 Å emission line. More recently, Grupe et al. (2010) have derived a *FWHM* of $1760 \pm 50 \text{ km s}^{-1}$ for H β , less than the value used as one of the criteria to distinguish Narrow Line Seyfert 1 (NLS1) from Seyfert 1 galaxies. Nevertheless, the objects was classified as a NLS1 by Véron-Cetty & Véron (2006). As in the case of UGC 11763 (Cardaci et al. 2009), Mrk 110 seems to be located in a transition zone between the Seyfert 1 and NLS1 classifications, showing some of the properties of each class.

In Table 1 we list the general characteristics of the galaxies in our sample as obtained from the literature: celestial coordinates (α_{2000} and δ_{2000}), redshifts (z), the distances in Mpc as derived from their redshifts using the expression $D = (cz/H_0)$ and adopting $H_0 = 75 \text{ km s}^{-1} \text{ Mpc}^{-1}$, and estimated Galactic hydrogen column densities (N_{H}) in the line of sights taken from Dickey & Lockman (1990).

The paper is organized as follows. In Sect. 2 we describe the observations and data reduction. The optical-UV results and the X-ray spectral analysis are presented in Sects. 3 and 5, respectively. In Sect. 4 we analyze the variability during the *XMM-Newton* observation and compare our observed fluxes with those from the literature. Our results are discussed in Sect. 6. And finally, the summary and conclusions of this work are given in Sect. 7.

2. Observations

ESO 359-G19, HE 1143-1810, CTS A08.12, and Mrk 110 were observed by *XMM-Newton* (Jansen et al. 2001) in 2004 (Table 2) as part of a project to characterize the complex profile of the iron K α line and the features that sometimes appear in the soft X-ray spectral range. The four galaxies of this study were selected to be brighter than 0.85 c s^{-1} in the ROSAT Bright Source Catalog (Voges et al. 1999) and not previously observed by the *XMM-Newton*. Exposure times were estimated from the available *ASCA* and ROSAT observations. The observing modes for EPIC-pn and EPIC-MOS1 (Turner et al. 2001) were selected according to the expected count rates (from PIMMS¹) to

¹ <http://cxc.harvard.edu/toolkit/pimms.jsp>

Table 2. Journal of observations.

Object	Observ. ID	Date
ESO 359-G19	02011301010	09 March 2004
HE 1143-1810	02011302010	08 June 2004
CTS A08.12	02011303010	30 October 2004
Mrk 110	02011305010	15 November 2004

avoid pile-up effects, and the selections are listed in Table 3. EPIC-MOS2 camera was always set in full frame mode to allow cross check for bright serendipitous X-ray sources in the field that could contaminate the RGS spectra. RGSs (den Herder et al. 2001) were run in the default spectroscopy mode. Optical Monitor (OM, Mason et al. 2001) observations that combined broad-band imaging filters were requested to investigate the circumnuclear structure in the UV domain with a series of UV-Grism exposures to obtain UV spectral and variability information about the active nucleus.

The OM, when used with broad-band filters, was always operated with the “science user defined” windows mode. The OM windows were centered on the target, with no spatial binning to maximize the resolution and with the maximum allowed size for those windows that is $5'1 \times 5'0$. This mode is the best choice for galaxies that are small enough to be fully included in a few arcmin square window. The default OM windows are designed to provide data over the whole OM field of view which, because it is larger, needs more time to be fully covered. The default grism window was selected for using the OM with the UV grism. This window contains the zeroth-order image and the first-order spectrum of the target at full detector resolution. More details on the EPIC and OM operating modes can be found in the *XMM-Newton Users Handbook* (2010).

The data were processed with the 8.0.0 version of the Science Analysis Subsystem (SAS) software package (Jansen et al. 2001) using the calibration files available in January 2009. All the standard procedures and screening criteria were followed for extracting the scientific products.

2.1. Selection of low background intervals

High background time intervals have been excluded using the method that maximizes the signal-to-noise in the spectrum (MaxSNR) as described in Piconcelli et al. (2004). The observations of ESO 359-G19 and CTS A08.12 were affected by an increase in the background radiation towards the end of the observation. The periods affected by high radiation were not taken into account for the EPIC-MOS spectral extraction. There was no need, however, to reject any time interval from the EPIC-pn data of any of either source. For ESO 359-G19, time intervals with background count rates higher than 0.6 and 3.2 c s^{-1}

Table 3. Details of *XMM-Newton* instrument exposures.

Instrument	Mode	Filter	Time (s) Scheduled	Time (s) Effective
ESO 359-G19				
EPIC-pn	Small Window	Thick	23 964	16 804 ^a
EPIC-MOS1	Small Window	Thin	24 157	19 375
EPIC-MOS2	Full Frame	Medium	24 172	23 908
RGS1	Spectroscopy	–	24 385	23 968
RGS2	Spectroscopy	–	24 380	23 953
OM	Image ^b	<i>U</i>	1300	
OM	Image ^b	<i>U</i>	1200	
OM	Image ^b	<i>B</i>	2 × 1200	
OM	Image ^b	<i>UVW1</i>	2 × 1400	
OM	Image ^b	<i>UVM2</i>	1500	
OM	Image ^b	<i>UVM2</i>	1400	
OM	Image ^b	<i>UVW2</i>	2 × 1800	
OM	Image ^b	UV Grism	4 × 1400	
HE 1143-1810				
EPIC-pn	Small Window	Thin	30 964	21 717 ^a
EPIC-MOS1	Small Window	Thin	31 157	29 660
EPIC-MOS2	Full Frame	Medium	31 172	30 253
RGS1	Spectroscopy	–	31 385	30 913
RGS2	Spectroscopy	–	31 380	30 887
OM	Image ^b	<i>U</i>	2 × 1200	
OM	Image ^b	<i>B</i>	2 × 1300	
OM	Image ^b	<i>UVW1</i>	2 × 1300	
OM	Image ^b	<i>UVM2</i>	2 × 1400	
OM	Image ^b	<i>UVW2</i>	2 × 1500	
OM	Image ^b	UV Grism	2 × 1200	
OM	Image ^b	UV Grism	7 × 1300	
CTS A08.12				
EPIC-pn	Small Window	Thin	45 964	32 089 ^a
EPIC-MOS1	Small Window	Thin	46 157	42 584
EPIC-MOS2	Full Frame	Medium	46 172	44 787
RGS1	Spectroscopy	–	46 385	45 841
RGS2	Spectroscopy	–	46 380	45 817
OM	Image ^b	<i>V</i>	2 × 1200	
OM	Image ^b	<i>U</i>	2 × 1200	
OM	Image ^b	<i>B</i>	2 × 1200	
OM	Image ^b	<i>UVW1</i>	3 × 1400	
OM	Image ^b	<i>UVW1</i>	2 × 3200	
OM	Image ^b	<i>UVW1</i>	4 × 1200	
OM	Image ^b	<i>UVM2</i>	2 × 2000	
OM	Image ^b	<i>UVW2</i>	2 × 2500	
OM	Image ^b	UV Grism	2 × 4000	
Mrk 110 ^c				
EPIC-pn	Small Window	Thin	46 964	32 861 ^a
EPIC-MOS1	Small Window	Thin	47 157	45 656
EPIC-MOS2	Full Frame	Medium	47 172	46 554
RGS1	Spectroscopy	–	47 385	47 189
RGS2	Spectroscopy	–	47 380	47 152
OM	Image ^b	<i>V</i>	2 × 1200	
OM	Image ^b	<i>U</i>	2 × 1300	
OM	Image ^b	<i>B</i>	2 × 1300	
OM	Image ^b	<i>UVW1</i>	10 × 1400	
OM	Image ^b	<i>UVM2</i>	2 × 2000	
OM	Image ^b	<i>UVW2</i>	2 × 2500	
OM	Image ^b	UV Grism	4000	
OM	Image ^b	UV Grism	2160	

Notes. ^(a) The live time of the EPIC-pn small window mode is 0.71. ^(b) In the science user defined mode. ^(c) Observation was offset for calibration purposes.

had to be discarded from the EPIC-MOS1 and EPIC-MOS2 spectra, respectively. The total discarded time was about 5%

for EPIC-MOS1 and about 1.5% for EPIC-MOS2 of the total observing time. In the case of CTS A08.12, time intervals with background count rates higher than 0.9 and 0.5 c s⁻¹ were subtracted of EPIC-MOS1 and EPIC-MOS2, respectively. The total discarded time was about 2.5% and much less than the 1% of the total observing time for EPIC-MOS1 and EPIC-MOS2, respectively.

No high background intervals occurred during the HE 1143-1810 and Mrk 110 observations. Therefore, the EPIC-pn spectrum of HE 1143-1810 and all the EPIC spectra of Mrk 110 did not need to be cut in time. Nevertheless, as a result of applying the MaxSNR procedure, time intervals with background count rates higher than 0.4 c s⁻¹ had to be discarded from both EPIC-MOS spectra of HE 1143-1810. The total discarded time was about 1.5% of the total observing time in each case.

The light curves of the RGS background radiation corresponding to our data show a significant increase towards the end of the ESO 359-G19 observation, reaching even >1 c s⁻¹ for RGS2, whose sensitivity is slightly greater than that of RGS1. Approximately the first 19 ks of the observation had a background count rate below 0.2 c s⁻¹, and then it increased (in average) to about 0.4 c s⁻¹. During the observations of HE 1143-1810 and Mrk 110, the background count rates of the RGS spectra were less than 0.2 c s⁻¹. Despite the increase in the background radiation that occurred during the ESO 359-G19 and CTS A08.12 observations, it was unnecessary to exclude the periods of increased background radiation since it always remained between 0.1 and 1.3 counts per second, which is considered normal (*XMM-Newton SAS Users Guide 2004*).

Detailed instruments configurations are given in Table 3 for each object. The last column of this table lists the final effective exposure time after taking the live time² into account.

3. Optical-UV analysis

OM data were processed with the SAS task OMICHAIN and default parameters. In the broad-band OM images, there is no clear evidence of extended emission. The images provide flux measures in the selected filters: *B*, *U*, *UVW1*, *UVM2*, and *UVW2* for all objects and also *V* for CTS A08.12 and Mrk 110. Table 4 shows the effective wavelengths of these filters, together with measured fluxes. When more than one exposure per filter is available, the mean value is listed. The flux differences on each series of consecutive exposures with the same filter are all compatible with no variability within the measurement errors (<3%).

The spectrum recorded in each individual UV-grism exposure is very weak; in addition, a number of zero-order images near the spectrum location and along the dispersion further complicate the extraction of the source spectrum. As a result, the total signal-to-noise of the extracted spectra was not as high as expected.

HE 1143-1810 was observed by the International Ultraviolet Explorer (IUE) in three different epochs between 1987 and 1990 with its Short Wavelength (1150–1950 Å) and Long Wavelength (1950–3200 Å) spectrographs. OM flux measurements in the *UVW2*, *UVM2*, and *UVW1* filters are overplotted in the top

² The live time is the ratio between the time interval during which the CCD is collecting X-ray events (integration time, including any time needed to shift events towards the readout) and the frame time (which in addition includes time needed for the readout of the events). *XMM-Newton Users Handbook* (http://xmm.esac.esa.int/external/xmm_user_support/documentation/uhb/node28.html).

Table 4. Fluxes in the OM filters obtained using aperture photometry.

Filter	V	B	U	$UVW1$	$UVM2$	$UVW2$
	λ_{eff} 5430 Å	4500 Å	3440 Å	2910 Å	2310 Å	2120 Å
ESO 359-G19	–	1.43 ± 0.01	1.34 ± 0.01	1.96 ± 0.03	1.86 ± 0.06	1.7 ± 0.10
HE 1143-1810	–	7.65 ± 0.02	15.82 ± 0.03	19.68 ± 0.05	24.4 ± 0.10	26.8 ± 0.40
CTS A08.12	1.78 ± 0.02	1.60 ± 0.02	2.31 ± 0.02	2.80 ± 0.01	3.00 ± 0.07	2.6 ± 0.10
Mrk 110	5.75 ± 0.03	7.30 ± 0.02	14.16 ± 0.03	17.53 ± 0.02	22.4 ± 0.10	24.8 ± 0.30

Notes. Fluxes are the mean values of the multiple exposures on each filter and are given in 10^{-15} erg cm^{-2} s^{-1} Å $^{-1}$ units.

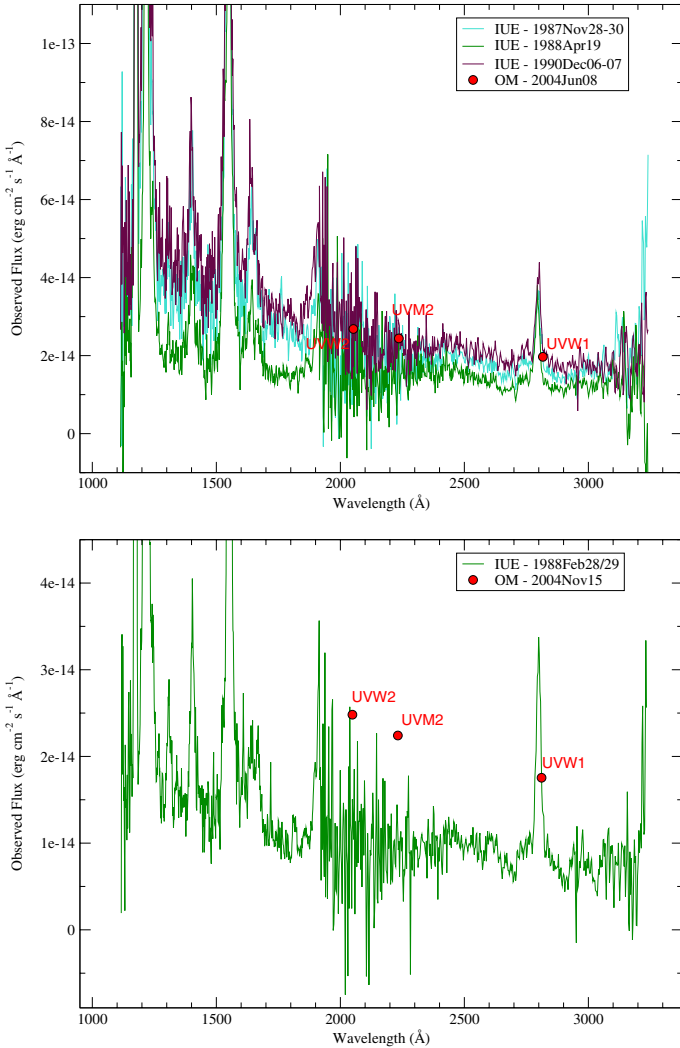


Fig. 1. Average IUE spectra (1200–3200 Å) of HE 1143-1810 (top) for the three observing epochs, and Mrk 110 (bottom) for the observing epoch. Solid red circles show the OM measures for the $UVW2$, $UVM2$, and $UVW1$ filters.

panel of Fig. 1 on the average IUE spectra of each epoch. In this figure we see that the average UV spectrum taken in 1990 is indeed an acceptable representation of the UV spectral energy distribution (SED) of HE 1143-1810 at the time of the *XMM-Newton* observation. From the IUE average spectrum in the rest frame we took the UV flux at 2500 Å, $F(2500 \text{ Å}) = 2.2 \times 10^{-14}$ erg cm^{-2} s^{-1} Å $^{-1}$. This value has been corrected for neither the Balmer continuum nor the FeII contributions.

Mrk 110 was also observed by the IUE in 1988 with its Short Wavelength and Long Wavelength spectrographs. Figure 1 (bottom panel) shows the average IUE spectrum with the fluxes

obtained from the OM filters overplotted. This figure shows that Mrk 110 was in a lower flux state when observed by IUE than when observed by *XMM-Newton*. After comparing the fluxes obtained for the OM filters $UVM2$ and $UVW1$ with those from the IUE observation for the same wavelengths, we estimated that the difference between them is about 1×10^{-14} erg cm^{-2} s^{-1} Å $^{-1}$. Adding this value to the flux at 2500 Å obtained from the IUE average spectrum in the rest frame and assuming that the shape of the UV continuum is essentially the same for the different epochs (as in the case of HE 1143-1810), we estimate that $F(2500 \text{ Å}) = 2.05 \times 10^{-14}$ erg cm^{-2} s^{-1} Å $^{-1}$ at the time of our observation.

4. Variability

We analyzed the EPIC-pn soft (0.5–1 keV) and hard (2–10 keV) X-ray background-subtracted light curves to investigate the variability of the four observed sources during their *XMM-Newton* observations. The overall behavior of the light curves of ESO 359-G19 and CTS A08.12 seems to show a constant average flux value and short-time, low-amplitude flux variations. In the case of the ESO 359-G19 light curves (upper panel of Fig. 2), the ratio between the maximum and minimum count rates is $1.5^{+0.3}_{-0.2}$ and $1.3^{+0.3}_{-0.2}$ for the soft and hard bands, respectively, thereby indicating no statistically significant variations.

For CTS A08.12 light curves (lower panel of Fig. 2), the ratios of the maximum to minimum rate are 1.3 ± 0.1 and 1.4 ± 0.2 for soft and hard bands, respectively. Therefore, taking the typical flux variations of this kind of objects into account, the flux variation during the observation was of small amplitude although significant (3σ) in the soft band, and only marginally significant (2σ) in the hard band. Under a careful visual inspection of the light curves, there seems to be an anti-correlation between the variations in the soft and hard light curves: an increment in flux in the soft band seems to correspond to a decrement in the hard band flux, and *viceversa*. The cross-correlation function between these curves does not suggest that this behavior could be explained by a temporal delay. The soft vs. hard count rates representation shows a weak negative regression that could indicate an anti-correlation. However, there is a large dispersion in the data, so we cannot assert the presence of that anti-correlation based only on the present observations.

The light curves of HE 1143-1810 and Mrk 110 are not well modeled by a constant flux function. In the case of HE 1143-1810 the ratios between the maximum and minimum count rates are 1.10 ± 0.04 and 1.18 ± 0.07 , indicating that the flux variations are small but significant at the $\sim 2.5\sigma$ level (Fig. 3, upper panel). Flux variations in the two bands are well correlated without any temporal delay. For Mrk 110 the ratio between the maximum and minimum count rates for the soft and hard light curves (1.16 ± 0.04 and 1.23 ± 0.07) indicates that the amplitudes of the flux variations are small but significant at 4σ and 3σ levels, respectively (Fig. 3, lower panel). In this case, there is a time

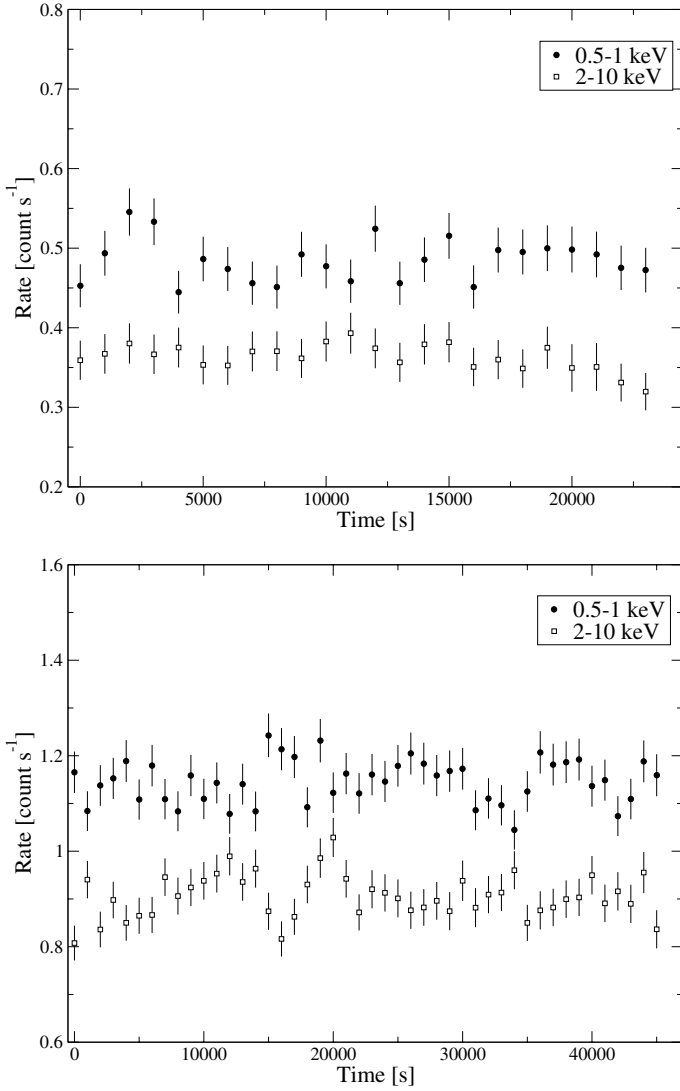


Fig. 2. Soft (filled circles) and hard (open squares) EPIC-pn light curves of ESO 359-G19 (*upper panel*) and CTS A08.12 (*lower panel*) binned by 1000 s.

lag of about 1000 s between the flux variations in the soft and hard bands, indicating that variations are seen first in the soft band and about 17 min later in the hard band.

The X-ray fluxes available from the literature for these objects are summarized in Table 5. For this table we have taken the fluxes listed as Flux1 in the ROSAT All-Sky Bright Source Catalog (Voges et al. 1999) since it is obtained assuming a power law model ($\alpha_x = 1.3$) with an absorbed column density fixed at the Galactic value. Fitting also an absorbed power law to the same ROSAT All-Sky Survey (RASS) data of ESO 359-G19 and Mrk 110, Grupe et al. (2004) found very different flux values (lower than those in Voges et al. 1999, by factors of about 2.2 and 1.7, respectively) in almost the same interval. All these objects show a variation of large amplitude in its soft X-ray flux, from a factor of about 2 for HE 1143-1810 to a factor of about 18 for ESO 359-G19. Fluxes in the 0.1–2.4 keV range taken from ROSAT observations 14 years before the *XMM-Newton* ones, are found to be larger than measured by us by about one order of magnitude for ESO 359-G19 and CTS A08.12 and by only a factor of 2 for HE 1143-1810. However, in the case of Mrk 110, our estimation of this flux is larger than the one obtained from ROSAT by a factor of 1.7. For this object the maximum soft

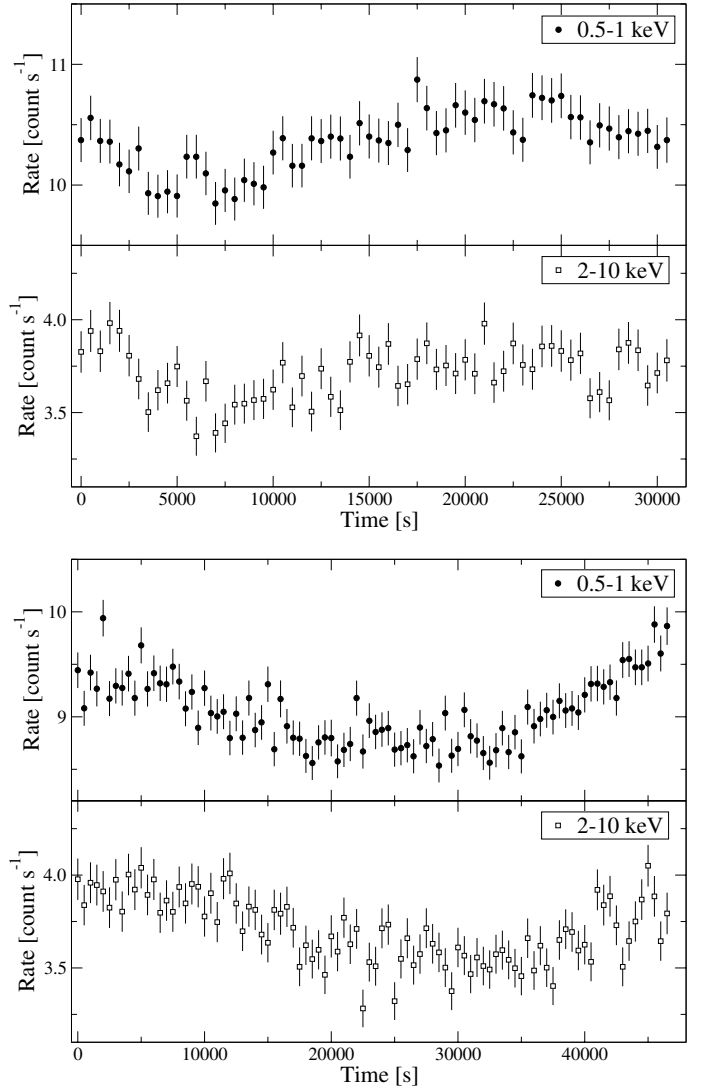


Fig. 3. Soft (filled circles) and hard (open squares) EPIC-pn light curves of HE 1143-1810 (*upper panel*) and Mrk 110 (*lower panel*) binned by 500 s.

X-ray flux reported in the literature was measured one year later (1991), also with ROSAT, and is a factor ~ 1.6 higher than our *XMM-Newton* value.

Swift observations exist for ESO 359-G19, HE 1143-1810, and Mrk 110. For the first, similar values to those derived by us are reported. In the case of HE 1143-1810 and Mrk 110 our results are higher and lower than those derived from the Swift data by factors of 2.5 and 1.5, respectively. Mrk 110 shows very similar flux values between the data acquired in 1991 and 2010 by ROSAT and Swift, respectively.

In the 2–10 keV range the amplitude of the flux variations is larger than a factor of 2 for HE 1143-1810 and 3.8 for CTS A08.12. For ESO 359-G19 there are no published data in this spectral range, and the hard *XMM-Newton* (2004) and *ASCA* (1998) values for Mrk 110 are very similar, although the *ASCA* soft flux is a factor ~ 1.4 lower than the soft *XMM-Newton* flux. Unfortunately, for the galaxies studied here there is no data in the hard spectral range taken contemporaneously to the observed highest soft X-ray flux. Taking the fluxes in Table 5 into account for these objects, it becomes clear that, when they were observed by the *XMM-Newton* satellite, only CTS A08.12 was in the lowest reported activity state, ESO 359-G19 was almost

Table 5. Comparison between X-ray fluxes from the literature and from this work.

Data	Obs. date	0.2–2 keV	0.5–2 keV	0.1–2.4 keV	2–10 keV	Ref.
ESO 359-G19						
ROSAT	1990 Aug.	–	–	48.3	–	1
ROSAT	1990 Aug.	21.9	–	–	–	2
XMM	2004 Mar.	2.39 ± 0.07	1.73 ± 0.05	2.71 ± 0.09	3.1 ± 0.1	3
Swift	2008 Oct. 12	2.8	–	–	–	4
Swift	2008 Oct. 26	2.0	–	–	–	4
HE 1143-1810						
ROSAT	1990 Dec.	–	–	75.8	–	1
XMM	2004 Jun.	–	–	–	28.3	5
XMM	2004 Jun.	37.69 ± 0.05	25.26 ± 0.05	40.72 ± 0.07	29_{-3}^{+1}	3
Swift	2006 Jul.	–	10.0	–	14.3	6
CTS A08.12						
ROSAT	1990 Oct.	–	–	44.4	–	1
ASCA	1998 May	–	14.0	–	29.0	7
XMM	2004 Oct.	4.07 ± 0.05	3.31 ± 0.05	4.66 ± 0.06	7.6 ± 0.1	3
Mrk 110						
ROSAT	1990 Oct.	–	–	23.0	–	1
ROSAT	1990 Oct.	13.8	–	–	–	2
ROSAT	1991 Oct.	55.0	–	–	–	2
ASCA	1998 May	–	16.0	–	28.0	7
XMM	2004 Nov.	–	–	–	28.5	5
XMM	2004 Nov.	–	–	–	28	8
XMM	2004 Nov.	35 ± 3	22 ± 3	38 ± 4	29 ± 2	3
Swift	2010 Jan. 06	51.3	–	–	–	4
Swift	2010 Jan. 12	52.4	–	–	–	4

Notes. Fluxes are given in 10^{-12} erg cm^{-2} s^{-1} . Errors quoted are at 90% confidence level.

References. (1) [Voges et al. \(1999; Flux1\)](#); (2) [Grupe et al. \(2001\)](#); (3) this work; (4) [Grupe et al. \(2010\)](#); (5) [Nandra et al. \(2007\)](#); (6) [Winter et al. \(2009\)](#); (7) from the TARTARUS database (<http://tartarus.gsfc.nasa.gov/>); (8) [de Marco et al. \(2009\)](#).

in the lowest reported state (very similar to Swift observations), and HE 1143-1810 and Mrk 110 were in an intermediate state.

5. X-ray spectral analysis

All the EPIC data were checked for no pile-up effects using the SAS task EPATPLOT. We have found these effects to be present in the EPIC-MOS1 and EPIC-MOS2 spectra of HE 1143-1810 and Mrk 110. For these objects we excised the core of the source (i.e., the core of the point spread function) using an annular shape for the source extraction region of the MOS data. The inner radii were selected as the minimum radii that ensures a negligible fraction (less than 5%) of pile-up in the data. The EPIC spectra were extracted using standard parameters. Except for those data affected by pile-up, the source extraction areas were circular regions. All the EPIC spectra were binned to have at least 30 counts per bin.

The RGS data were processed with default parameters except that we discarded potentially problematic cold pixels. All the RGS spectra were binned, losing spectral resolution but increasing the signal-to-noise ratio. We selected a geometrical binning since this method minimizes any smoothing of the absorption and emission features. We binned the RGS data of ESO 359-G19, HE 1143-1810, and CTS A08.12 using 15 channels per bin, while 10 channels per bin were used in the case of Mrk 110. Because the default RGS spectral bin size is $10 \text{ m}\text{\AA}$ at 15 \AA , our final spectra for ESO 359-G19, HE 1143-1810, and CTS A08.12 have bins of about $150 \text{ m}\text{\AA}$ at that wavelength, while those of Mrk 110 have bins of about $100 \text{ m}\text{\AA}$.

All spectra were fitted using *Sherpa* package of *CIAO 3.4* ([Freeman et al. 2001](#); [Silva & Doxsey 2006](#)). We used the χ^2

statistics with the Gehrels variance function ([Gehrels 1986](#)) and the Powell optimization method, the first because it is based on Poisson statistics for a small number of counts in a bin and on Binomial statistics otherwise, and the second because it is a robust direction-set method for finding the nearby fit-statistical minimum.

5.1. Low-resolution spectra

For each source we start by fitting only the EPIC-pn spectrum in the hard band (2.0–10.0 keV), then we check for soft excess extending the hard band model to the soft band, and finally we fit the three EPIC (pn, MOS 1 and MOS 2) spectra simultaneously in the whole range considered (0.35–10 keV). Below 1 keV, all the objects analyzed in this work show an X-rays excess over the extrapolation of the harder power law flux. Soft excess components are modeled in the simplest way. We first use a black body component, and in the case this model does not represent the observed excess, we use a power law. Because the Galactic absorption has to be taken into account, we include, in all the source models mentioned from here on, a component that models the Galactic neutral absorption with the hydrogen column density (N_{H}) fixed to the values listed in Table 1. In Table 6 we list – for each source – the best-fit model continuum parameters found by performing the simultaneous EPIC fit.

The criteria we have used to include Gaussian profiles in the models is the same as described in [Cardaci et al. \(2009\)](#). The lines are added constraining their energies to vary in a small range around their laboratory energies (E_{lab}) and taking the redshift of the source into account. Since we cannot use only the F-test as a reliable criterion to compute the statistical

Table 6. Best-fit model to the continuum of the EPIC spectra in the 0.35–10 keV range.

	Hard power law		Black body		Soft power law		$\chi^2_v/\text{d.o.f.}$
	Γ	K_{plw}	kT	K_{bb}	Γ	K_{plw}	
ESO 359-G19	$1.69^{+0.04}_{-0.04}$	$7.1^{+0.3}_{-0.3}$	$0.16^{+0.01}_{-0.01}$	$7.1^{+0.3}_{-0.3}$	—	—	0.76/716
HE 1143-1810	$1.19^{+0.07}_{-0.07}$	19^{+3}_{-3}	—	—	$2.61^{+0.03}_{-0.03}$	102^{+3}_{-3}	0.90/1914
CTS A08.12	$1.55^{+0.02}_{-0.02}$	$14.5^{+0.2}_{-0.2}$	$0.131^{+0.004}_{-0.004}$	$1.46^{+0.09}_{-0.09}$	—	—	0.88/1486
Mrk 110	$1.3^{+0.2}_{-0.1}$	24^{+21}_{-5}	—	—	$2.5^{+0.3}_{-0.1}$	78^{+5}_{-12}	0.90/2187

Notes. Power-law normalizations (K_{plw}) in units of 10^{-4} ph keV $^{-1}$ cm $^{-2}$ s $^{-1}$ at 1 keV; kT in keV; K_{bb} in $10^{-5} L_{39}/D_{10}^2$ where L_{39} is the source luminosity in units of 10^{39} erg s $^{-1}$ and D_{10} is the distance to the source in units of 10 kpc. The Galactic N_{H} values are fixed (see Table 1). Errors quoted are at 90% confidence level.

significance of a Gaussian line (Protassov et al. 2002), we use a combined method to decide whether to include a line in our final model. Along with the F-test, for which the minimum significance level considered is 95%, we check that the residuals of the new fit at the position of the tested line is less than 1 sigma, and finally we also ensure that the wavelength positioning of the line be consistent with its laboratory wavelength (taking the galaxy redshift into account).

Except for Mrk 110, we find that the fluorescent Fe-K α emission line is significant to the fit (with more than 99% significance). The Fe-K α line widths, σ , are small enough to be considered equal to the instrumental resolution.

After analyzing the residuals of the ESO 359-G19 fit, we find a second narrow line at about 7 keV that could be originated by FeXXVI ($E_{\text{lab}} = 6.966$ keV). The line width has been fixed to the instrumental resolution. This line is statistically significant to the fit (with more than 95% significance).

In the residuals of the HE 1143-1810 fit, we see a wide 4σ Gaussian shape excess between 0.4 and 0.8 keV. This excess is well described with a Gaussian line centered at $0.579^{+0.006}_{-0.007}$ keV (~ 21.4 Å) with a dispersion of $0.06^{+0.01}_{-0.01}$ keV ($28\,000^{+5000}_{-5000}$ km s $^{-1}$). It could be interpreted as a blend of OvII lines.

On the CTS A08.12 fit, there is still a small (2 sigma) line-like residual around 6 keV that might indicate a relativistic shape for the Fe-K α line. Unfortunately, the signal-to-noise ratio of this line is low, and with these data we cannot test the hypothesis of a potential relativistic shape of the Fe-K α line any further.

In the case of Mrk 110, although there are residuals around 6 keV that could be interpreted as signatures of an Fe-K α emission line, including this component (with only 70% significance) proved not to be significant to the fit. After the modeling of the soft excess component still remains a broad excess in the residuals between 0.5 and 0.6 keV. We included three Gaussian components at the energy position of the OvII triplet emission lines (0.5740, 0.5686, 0.5610 keV) to model it. These lines were included with the relative energies between them fixed to the theoretical values, and having the same dispersion. Since the normalizations of two of the lines take lower values (around 2×10^{-5} and 3×10^{-6} ph cm $^{-2}$ s $^{-1}$) than the third line (about 4×10^{-4} ph cm $^{-2}$ s $^{-1}$) this triplet is dominated by only one component.

The parameter values of the final EPIC model of each object are listed in Tables 6 and 7.

5.2. High-resolution X-ray spectra

The EPIC spectra, with their broad energy coverage provide a good picture of the shape of the continuum emission of the source and its wide emission features. However, the search for

Table 7. Line parameters included in the best-fit model to the simultaneous three EPIC spectra in the 0.35–10 keV range.

Object	Line	E_{lab}	E_{rest}	σ	K_{line}
ESO 359-G19	Fe K α	6.4	$6.38^{+0.06}_{-0.05}$	0.004^a	$0.7^{+0.2}_{-0.2}$
	FeXXVI	6.966	6.97^a	0^b	$0.5^{+0.2}_{-0.2}$
HE 1143-1810	Fe K α	6.4	$6.39^{+0.04}_{-0.04}$	$0.07^{+0.05}_{-0.04}$	$1.8^{+0.7}_{-0.6}$
	OvII	blend	$0.579^{+0.006}_{-0.007}$	$0.06^{+0.01}_{-0.01}$	90^{+10}_{-10}
CTS A08.12	Fe K α	6.4	$6.39^{+0.02}_{-0.03}$	$0.06^{+0.04}_{-0.04}$	$1.2^{+0.3}_{-0.3}$
Mrk 110	OvII (r)	0.5740	$0.59^{+0.12}_{-0.17}$	$0.05^{+0.03}_{-0.04}$	2.2^a
	OvII (i)	0.5686	0.5871^c	0.05^c	0.3^a
	OvII (f)	0.5610	0.5795^c	0.05^c	44^a

Notes. ^(a) Unconstrained. ^(b) Fixed to the instrumental resolution. ^(c) Fixed to the energy and width of the recombination component. E_{rest} (line energies in the rest frame of the source), E_{lab} and σ of the emission lines are given in keV; and line normalizations K_{line} in units of 10^{-5} ph cm $^{-2}$ s $^{-1}$. Errors quoted are at 90% confidence level.

narrow features requires using the higher resolution spectra provided by the RGS instruments. On the other hand, by fitting only the RGS spectra, one could find solutions not completely compatible with those derived from the analysis of the EPIC spectra alone. Therefore a comprehensive five-spectra fit including the three EPIC and the two RGS spectra has been made. The EPIC-pn and EPIC-MOS data are restricted to the 0.35–10 keV energy range, while the RGS data are taken in the 0.41 and 1.8 keV (about 6.9–30.2 Å) range.

The best-fitting model obtained using the low-resolution spectra is used as the first approximation for the five-spectra fit. No relevant intrinsic neutral absorption components associated with the studied sources have been found.

For the fit of ESO 359-G19 data we find a model with a hard power law ($\Gamma = 1.78^{+0.03}_{-0.05}$) slightly steeper than for the simple EPIC fit and with a lower black body temperature ($kT = 0.08^{+0.03}_{-0.04}$). The parameter values of the Fe lines identified on the EPIC spectra remain unchanged. In the residuals of the RGS fit (Fig. 4), we notice a wide feature located at about 20 Å. We tried to model it with a Gaussian component but we did not find a satisfactory solution. The best-fitting model is plotted in Fig. 4.

For HE 1143-1810, the same model that fits the EPIC-pn and EPIC-MOS data is also valid for describing the RGS data in the comprehensive fit ($\chi^2_v/\text{d.o.f.} = 0.92/2097$). When substituting the broad oxygen line by three lines to account for the OvII triplet, we find that the EPIC spectra are not well modeled at soft energies. Residuals show about 4σ departures from zero. We also tested for the presence of narrow OvII triplet lines including them

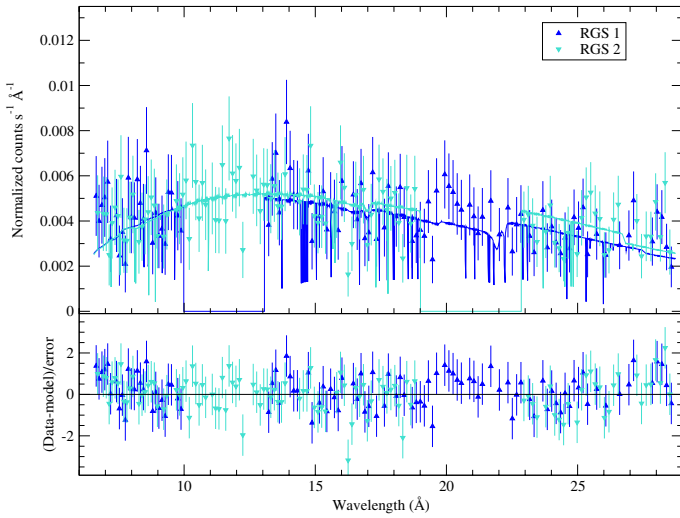
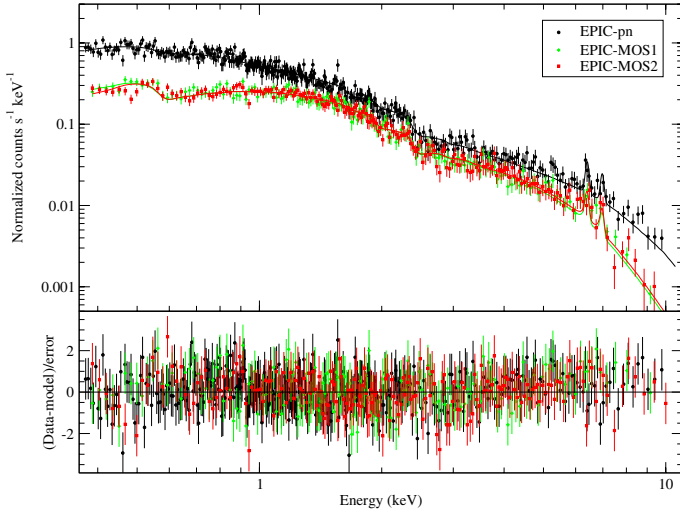


Fig. 4. ESO 359-G19. *Upper panel:* low-resolution X-ray spectra – in the rest frame – as obtained with the EPIC-pn (black dots), EPIC-MOS1 (green diamonds), and EPIC-MOS2 (red squares) cameras. The best-fit model after a comprehensive fit of the EPIC-pn, EPIC-MOS, and RGS spectra (Tables 8 and 9) convolved with the instrument response of each camera is shown as a solid line. *Lower panel:* high-resolution X-ray spectra – in the rest frame – as obtained with the RGS1 (blue up triangles), and RGS2 (cyan down triangles), and binned to 15 channels per bin. Solid lines are the convolution of the best-fit model after a comprehensive fit of the EPIC-pn, EPIC-MOS, and RGS spectra (Tables 8 and 9) with instrument responses.

only in the RGS spectra model but no satisfactory solution was found. Figure 5 shows the model and errors, together with the spectral data.

Also in the case of CTS A08.12, the same model provides a good fit to both the EPIC and the RGS data. However, the residuals in the high-resolution spectra fit indicate the need to introduce narrow Gaussian lines at the theoretical wavelengths of the O VII and O VIII lines. Only one of the O VII lines is found (the normalizations of the other two are lower than 10^{-9} ph cm $^{-2}$ s $^{-1}$ keV $^{-1}$), and it is significant to the fit (more than 99% confidence level). The O VIII emission line is not statistically significant to the fit. In this object, the wide feature in absorption that arises between 15 and 17 Å could be the signature of partially ionized material absorbing the source radiation. We tested for the possible presence of such a component using the PHASE photoionization code (Krongold et al. 2003) and find a hydro-

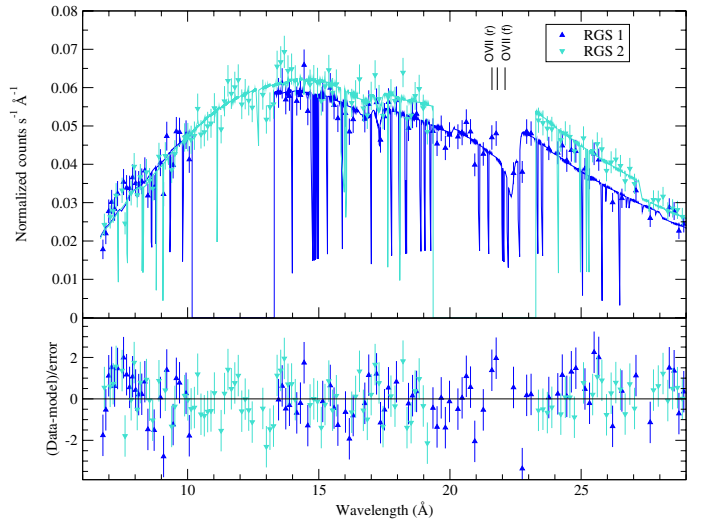
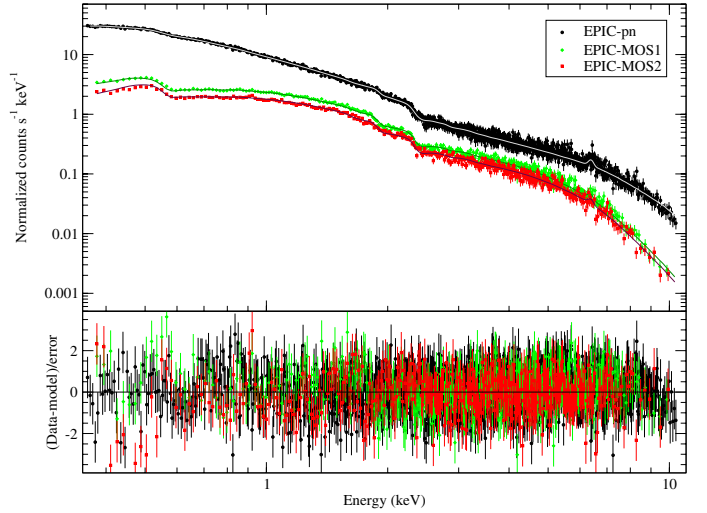


Fig. 5. As in Fig. 4 for HE 1143-1810.

gen column density lower than 10^{20} cm $^{-3}$ for the absorbing gas. Such a component does not affect the X-ray bands analyzed in the present work. The best-fitting model is plotted in Fig. 6.

The model that best reproduces the EPIC spectra of Mrk 110 leaves residuals on the RGS spectra that could come from the presence of narrow emission lines. Also departures 2σ larger than zero are found at ~ 6.4 keV that point to the presence of a weak Fe line. Although the addition of this line was found to not be statistically significant to the fit of the EPIC data, we decided to incorporate it in the five-spectra fit. This line was modeled with a Gaussian profile whose width was left free. As a result, a very broad feature ($\sigma \sim 2$ keV) centered on ~ 5 keV was obtained. Since the feature seen in the residuals is not very wide, we tried to find the best parameters for this line “by hand”. Then we realized that the line dispersion could be frozen to the instrumental resolution. With the initial parameters found in this way we get a satisfactory fitting for this Fe emission line at about 6.4 keV, although the fitting process is not able to find the errors associated with the energy value of the line. The narrow features that appear in the RGS data were modeled with a second O VII triplet (i.e., another set of three Gaussian lines linked in energies and dispersions) and an O VIII line. It should be emphasized that these lines were included only in the RGS model and that all of them turn out to be significant to the fit. Figure 7 shows the

Table 8. Continuum parameters of the comprehensive EPIC-pn, EPIC-MOS, and RGS best-fit model for ESO 359-G19, HE 1143-1810, CTS A08.12, and Mrk 110.

	Hard power law		Black body		Soft power law		$\chi^2_{\nu}/\text{d.o.f.}$
	Γ	K_{pwlw}	kT	K_{bb}	Γ	K_{pwlw}	
ESO 359-G19	$1.78^{+0.04}_{-0.05}$	$7.9^{+0.2}_{-0.4}$	$0.08^{+0.03}_{-0.04}$	$0.3^{+0.03}_{-0.2}$	–	–	0.78/921
HE 1143-1810	$1.22^{+0.07}_{-0.07}$	20^{+3}_{-3}	–	–	$2.62^{+0.03}_{-0.03}$	101^{+3}_{-3}	0.92/2097
CTS A08.12	$1.56^{+0.02}_{-0.02}$	$14.7^{+0.2}_{-0.2}$	$0.126^{+0.004}_{-0.004}$	$1.43^{+0.09}_{-0.09}$	–	–	0.91/1665
Mrk 110	$1.34^{+0.10}_{-0.07}$	28^{+9}_{-5}	–	–	$2.59^{+0.34}_{-0.09}$	75^{+4}_{-11}	0.89/2513

Notes. ^(a) Unconstrained. Power-law normalizations (K_{pwlw}) in units of 10^{-4} ph keV $^{-1}$ cm $^{-2}$ s $^{-1}$ at 1 keV; kT in keV; K_{bb} in $10^{-5} L_{39}/D_{10}^2$ where L_{39} is the source luminosity in units of 10^{39} erg s $^{-1}$ and D_{10} is the distance to the source in units of 10 kpc. Normalizations K_{pwlw} and K_{bb} correspond to the EPIC-pn spectrum. The galactic N_{H} values are fixed (see Table 1). Errors quoted are at 90% confidence level.

Table 9. Line parameters included in the comprehensive EPIC-pn, EPIC-MOS, and RGS best-fit model for ESO 359-G19, HE 1143-1810, CTS A08.12, and Mrk 110.

Objects	Line	E_{lab}	E_{rest}	σ	K_{line}
ESO 359-G19	Fe K α	6.4	$6.38^{+0.06}_{-0.05}$	0.004^a	$0.7^{+0.2}_{-0.2}$
	Fe xxvi	6.966	6.97^a	0^b	$0.5^{+0.2}_{-0.2}$
HE 1143-1810	Fe K α	6.4	$6.39^{+0.04}_{-0.04}$	$0.07^{+0.05}_{-0.04}$	$1.8^{+0.7}_{-0.6}$
	Ovii	blend	$0.578^{+0.006}_{-0.007}$	$0.056^{+0.010}_{-0.009}$	90^{+10}_{-10}
CTS A08.12	Fe K α	6.4	$6.40^{+0.02}_{-0.03}$	$0.06^{+0.04}_{-0.04}$	$1.2^{+0.03}_{-0.03}$
	Ovii (r)	0.5740	$0.574^{+0.003}_{-0.006}$	$0.005^{+0.005}_{-0.005}$	7^{+4}_{-4}
Mrk 110	Fe K α	6.4	6.43^a	0^b	$1.5^{+0.4}_{-0.5}$
	Ovii(r)	0.5740	$0.59^{+0.04}_{-0.16}$	$0.04^{+0.02}_{-0.02}$	1.6^a
	Ovii(i)	0.5686	0.5872^c	0.04^c	0.9^a
	Ovii(f)	0.5610	0.5796^c	0.04^c	40^{+30}_{-30}
	Ovii(r) ^d	0.5740	0.5669^a	0^b	7^{+13}_{-7}
	Ovii(i) ^d	0.5686	0.5615^c	0^b	20^{+50}_{-20}
	Ovii(f) ^d	0.5610	0.5539^c	0^b	7^{+8}_{-4}
Oviii ^d	0.6536	$0.652^{+0.004}_{-0.005}$	0^b	3^{+5}_{-3}	

Notes. ^(a) Unconstrained. ^(b) Fixed to the instrumental resolution. ^(c) Linked to have the same relative energy with respect to the recombination component than the laboratory lines of the Ovii. ^(d) Only in the RGS model. The line energies (E_{lab} and E_{rest}) and σ of the emission lines are given in keV; and line normalizations K_{line} in units of 10^{-5} ph cm $^{-2}$ s $^{-1}$. Errors quoted are at 90% confidence level.

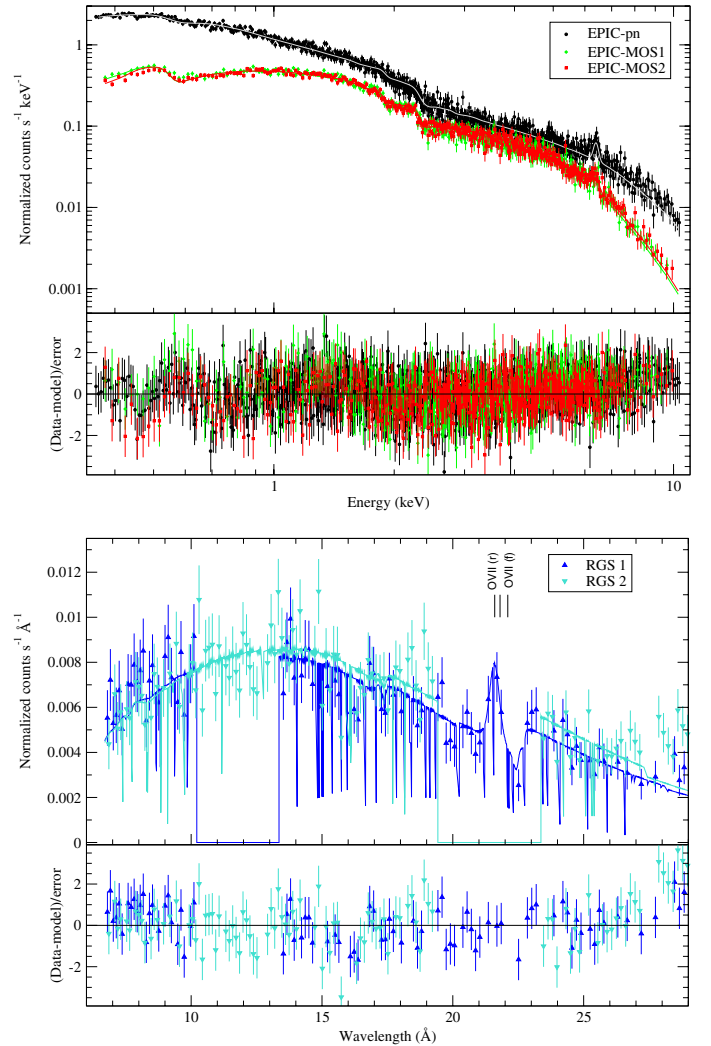
final model adopted for Mrk 110, along with the corresponding errors.

The parameter values of the best-fitting model for each of these objects are listed in Tables 8 and 9.

6. Discussion

UV emission

From the OM data of HE 1143-1810 we have found that the IUE average spectrum obtained in 1990 is representative of its flux state during the *XMM-Newton* observation. Using the IUE flux at 2500 Å and the flux at 2 keV from EPIC-pn data, $F(2 \text{ keV}) = 7.67 \times 10^{-12}$ erg cm $^{-2}$ s $^{-1}$ keV $^{-1}$, we obtain an optical/X-ray spectral index $\alpha_{\text{ox}} = 1.2$ for this object. This value is typical of Seyfert 1 AGNs, as shown by Wilkes & Elvis (1987) and Vasudevan & Fabian (2009).


Fig. 6. As in Fig. 4 for CTS A08.12.

In the case of Mrk 110, we have found that the IUE fluxes corresponding to the effective wavelengths of the OM filters *UVM2* and *UVW1* (λ 2310 and 2910 Å, respectively) seem to be lower than OM fluxes by 1×10^{-14} erg cm $^{-2}$ s $^{-1}$ Å $^{-1}$. Taking this correction into account we estimated the flux at 2500 Å that should correspond to the *XMM-Newton* observation. Using this estimate and the flux at 2 keV from EPIC-pn data, $F(2 \text{ keV}) = 7.28 \times 10^{-12}$ erg cm $^{-2}$ s $^{-1}$ keV $^{-1}$, we obtain an optical/X-ray spectral index $\alpha_{\text{ox}} = 1.2$ for this object, in very good agreement

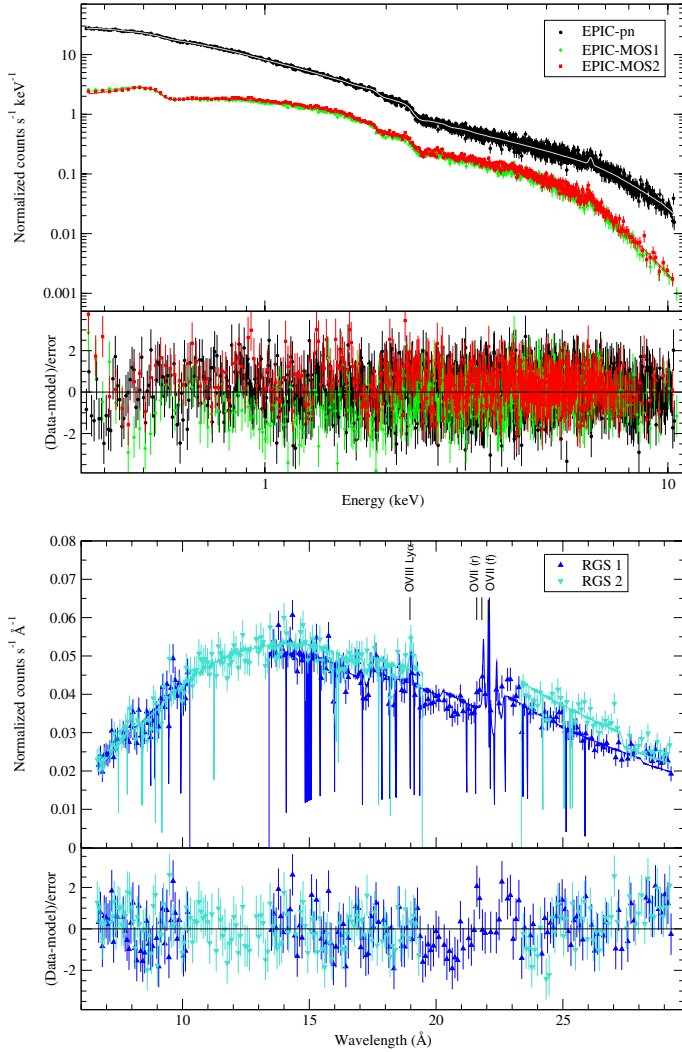


Fig. 7. As in Fig. 4 for Mrk 110.

with the one obtained by Vasudevan & Fabian (2009) using the same X-ray data.

Variability

The light curves of all the four objects analyzed in this work show low amplitude flux variations in the X-ray bands studied. ESO 359-G19 and CTS A08.12 are the sources with the lowest count rates. ESO 359-G19 shows only marginally significant variability in the soft band and no statistically significant variations in the hard band. The soft and hard band light curves are statistically well represented by constant fluxes with small variations of about 2 and 1 σ , respectively.

CTS A08.12 shows X-rays flux variations in both soft and hard bands, which are more significant for the former (3σ). Both light curves show a rather constant mean flux value. Under a careful visual inspection of the shape of the light curves, there seems to be an anti-correlation between the flux variations in the soft and hard bands. This anti-correlation, if real, could be interpreted in different ways (Ford et al. 1996):

- (i) thermal models (e.g., Sunyaev & Titarchuk 1980): when the soft X-ray flux increases, the Comptonizing plasma cools down, resulting in a decreased temperature and hard X-ray flux;

- (ii) non-thermal models: the soft and hard X-ray anti-correlation is the result of the suppression of particle acceleration by inverse Compton cooling caused by an enhanced soft X-ray background.

In HE 1143-1810 and Mrk 110, flux variations in the hard band follow the corresponding ones in the soft band with no lag between features in HE 1143-1810 and a delay of about 1000s (~ 17 min) in the case of Mrk 110 with the soft band variations preceding those in the hard band. This result is in very good agreement with the work of Dasgupta & Rao (2006), who did a detailed analysis of the variability during the same *XMM-Newton* observation. They reported the discovery of X-ray delays ranging from a few minutes to an hour between the light curves in seven selected spectral intervals (0.2–0.3, 0.3–0.42, 0.42–0.58, 0.58–0.8, 0.8–1.2, 1.2–2, and 2–12 keV). These authors explained the time lags as the effect of inverse Compton scattering by highly energetic electrons (a hot plasma; $T \sim 10^8$ – 10^9 K, Sunyaev & Titarchuk 1980) within about ten Schwarzschild radii of the black hole.

X-ray continuum emission

Regarding the shape of the continuum emission of the objects studied here, a power law accounts for the hard X-ray emission in all cases. The photon indices of ESO 359-G19 and CTS A08.12 have standard values between 1.5 and 2.5 for Seyfert 1s (Nandra & Pounds 1994; Reeves & Turner 2000; Piconcelli et al. 2005).

Analyzing *ROSAT* data of ESO 359-G19 (taken in 1990 with the source in a high flux state, in the 0.1–2.4 keV range), Grupe et al. (2001, 2004) fitted the soft X-ray continuum with a power law with a photon index of $\Gamma \sim 2.4$ that is consistent with the presence of the soft excess component. In Grupe et al. (2010), these authors analyzed *Swift* data (taken in 2008 with the source in low state) reporting that the continuum in the 0.3–10 keV range could be described with a power law with a photon index of $\Gamma \sim 1.7$. This value is consistent with the hard power law index, i.e. with no soft excess. The *XMM-Newton* data were also taken with the source in a low flux state. However, in contrast to the findings of Grupe and collaborators, we do not find the hard power law model sufficient for characterizing the continuum in the 0.3–10 keV range. In our case, a contribution by a soft excess component is found at energies lower than about 1 keV.

HE 1143-1810 and Mrk 110 have slightly lower photon indices than the ones typical of Seyfert 1s but they are still within the observed range of values for this kind of objects (Nandra & Pounds 1994; Reynolds 1997). Winter et al. (2009) fitted the 0.5–10 keV energy range of the *Swift* XRT data of HE 1143-1810 and the *ASCA* data of Mrk 110 using single power laws with photon indices of $\Gamma = 1.92 \pm 0.1$ and 1.78 ± 0.02 , respectively. In both cases the values derived are between the hard and soft power law photon indices obtained by us (see Table 8). However, in our observations we do not find that single power law models can be used to characterize the whole spectral range of the *XMM-Newton* data of these objects.

The Fe lines

In these four objects, we can see that a power law alone does not satisfactorily model the shape of the spectra in the 2–10 keV range. In all of them, an emission feature arises around 6.4 keV. This is the characteristic energy of the fluorescent neutral iron line, which is usually observed in the spectra of this kind of

objects. The iron emission line energy increases with increasing ionization. It is 6.4 keV for neutral Fe, 6.7 keV in the H-like Fe, and 6.966 keV in the He-like Fe (Krolik 1999). We used a Gaussian profile to characterize the energy, strength, and dispersion of the observed feature. For all the objects we find that this line is statistically significant to the fit, and the fitted energies are compatible – within the errors – with their being the neutral Fe $K\alpha$ line.

For the iron line dispersion, we find values of $0.07^{+0.05}_{-0.04}$ keV (3300^{+2300}_{-1900} km s⁻¹) for HE 1143-1810, $0.06^{+0.04}_{-0.04}$ keV (2800^{+1900}_{-1900} km s⁻¹) for CTS A08.12, and narrower than the instrumental resolution for ESO 359-G19 and Mrk 110. The equivalent widths (EW) of these lines are $0.16^{+0.12}_{-0.12}$ keV for ESO 359-G19, $0.07^{+0.04}_{-0.04}$ keV for HE 1143-1810, $0.14^{+0.06}_{-0.06}$ keV for CTS A08.12, and $0.05^{+0.02}_{-0.02}$ keV for Mrk 110.

The *XMM-Newton* data of HE 1143-1810 and Mrk 110 were included in the sample analyzed by Nandra et al. (2007) to study the Fe $K\alpha$ line observed in 26 Seyfert galaxies. For the iron line identified in the HE 1143-1810 data, they reported a central energy of $5.53^{+0.14}_{-0.22}$ keV (errors are given at the 68% confidence level). This energy is redshifted with respect to the laboratory energy of the neutral iron $K\alpha$ line. Moreover, the line they found is broader ($\sigma = 0.14^{+0.24}_{-0.14}$ keV, i.e., about 7600 km s⁻¹) than our estimation, and the EW (of 30^{+28}_{-21} eV) is about half our value. All these reasons, and a careful inspection of Fig. 3 of Nandra et al. (2007) lead us to think that the feature they fitted with a Gaussian profile is not the Fe $K\alpha$ line.

In the case of Mrk 110, Nandra et al. (2007) found the iron line at a central energy of $6.53^{+0.14}_{-0.11}$ keV. Taking the errors into account, this feature is compatible with the neutral fluorescent iron line at 6.4 keV, hence also with our estimation. The width ($\sigma = 0.00^{+0.23}_{-0.00}$ keV) of the line reported by these authors is in good agreement with our value, and their EW (17^{+41}_{-12} eV) is about 2.5 times lower than our estimation, but is also compatible within the errors. Boller et al. (2007) have also analyzed the same *XMM-Newton* observation of Mrk 110. They found similar parameters for the Fe line profile: a narrow line (with the line width unresolved within the energy resolution of the EPIC-pn detector), a central energy of $6.4^{+0.02}_{-0.04}$ keV, and an EW of 52^{+18}_{-16} eV. Our line parameters are also in good agreement with those more recently given by de Marco et al. (2009): $E_{\text{Fe}} = 6.41 \pm 0.04$ keV, $\sigma < 0.13$ keV, and $EW = 46 \pm 131.4$ eV.

In the ESO 359-G19 spectra, we have also identified a second narrow line in the hard band with an energy of ~ 6.97 keV, probably originated by highly ionized iron. This line has not been previously identified in the spectra of this source, but it has been reported in other Seyfert 1s, e.g., by Longinotti et al. (2007) in MKN 590 and Bianchi et al. (2008) in NGC 7213.

Soft excess

The extrapolation of the hard X-ray models of the four sample objects to lower energies, down to 0.35 keV, reveals the existence – in all of them – of a soft-X-ray flux in excess of this extrapolation, from ~ 2 keV and below. This excess was previously reported only for Mrk 110 (Boller et al. 2007). After testing the most typical components used to model the soft excess, we find that in ESO 359-G19 and CTS A08.12 it can be accounted for with a black body component with $kT = 0.08^{+0.03}_{-0.04}$ and $kT = 0.126^{+0.004}_{-0.004}$ keV, respectively. On the other hand, for HE 1143-1810 and Mrk 110, a (soft) power law is the model that best accounts for the observed soft excess with photon indices of

$2.62^{+0.03}_{-0.03}$ and $2.59^{+0.34}_{-0.09}$, respectively. Both the values of the kT of the black bodies and the slopes of the power laws found by us are consistent with the values found in many other Seyfert galaxies (Picconcelli et al. 2005).

Grupe et al. (2001) analyzed the ROSAT data of ESO 359-G19 in the 0.2–2 keV energy range. These authors use a power law with a photon index $\Gamma = 2.41 \pm 0.07$ to describe the continuum emission in the soft band. This is a characteristic value for AGNs with a small-amplitude soft excess as is the case of ESO 359-G19. In a recent work, Grupe et al. (2010) using two Swift observations data in the same soft band (0.2–2 keV) found soft power law photon indices of 1.72 ± 0.10 and 1.60 ± 0.14 , which are more typical of the spectral indices observed in the 2–10 keV energy band. This behavior could indicate that the soft excess is variable both in flux and shape as seen in NLS1 objects.

ROSAT data of Mrk 110 were also analyzed by Grupe et al. (2001). They found a photon index of 2.29 ± 0.09 for the energy range of 0.2–2 keV, slightly lower than our value. Using a more complex model than ours to analyze the same observation, Boller et al. (2007) also found a good description of the soft X-ray excess with a power law with a photon index of $2.5^{+0.13}_{-0.02}$, which is in very good agreement with the value we find. It must be noticed that another component of their model, mainly a starburst, also contributes to the soft X-ray emission, as discussed below.

Broad soft X-ray features

After the EPIC spectra of HE 1143-1810 and Mrk 110 were modeled with two power laws and an Fe Gaussian component at about 6.4 keV, the residuals of the fit clearly show that the models underestimate the counts around 0.5–0.6 keV. The residuals have a Gaussian-like shape and arise in the range in which the Ovii laboratory energies lay (0.5740, 0.5686, 0.5610 keV). These energies are also covered by the RGS spectrometers, so the features seen in the EPIC soft X-rays range should also be seen in the RGS spectra.

For HE 1143-1810, a Gaussian profile ($\sigma = 0.056^{+0.010}_{-0.009}$ keV, i.e., 29000^{+5000}_{-5000} km s⁻¹) accounts for the broad feature seen in the EPIC and RGS spectra with a central energy of $0.578^{+0.006}_{-0.007}$ keV ($21.5^{+0.2}_{-0.2}$ Å). This line energy is compatible within the errors with the resonant line of the Ovii. The RGS data does not show any other significant feature that indicates emission or absorption.

In the case of Mrk 110, a similar single broad Gaussian profile does not account for the observed feature either in the EPIC data or in the RGS data. To achieve a good description of the broad and narrow emission features that arise in the EPIC and RGS spectra, respectively, we have included in the model some Gaussian profiles. Three broad profiles account for the broad excess in the EPIC data. Since we assume that these lines are produced by the Ovii-He α triplet, we fixed their relative energies to the laboratory values. In this way we find the lines at energies of $0.59^{+0.04}_{-0.16}$, 0.5872, and 0.5796 keV (21, 21.1 and 21.4 Å). The line widths were also forced to be the same for the three lines obtaining dispersions of $\sigma = 0.04^{+0.02}_{-0.02}$ keV, equivalent to 20000^{+10000}_{-12000} km s⁻¹. Regarding the width and intensities, we can see that the lines overlap and the third one dominates the profile, although we notice that the normalizations are unconstrained (Table 9). Line energies are highly blueshifted, $z \sim -0.034$, when taking the Mrk 110 redshift into account ($z \sim 0.035$). Since these two values are almost equal (in absolute value), this implies that the broad feature, if it is associated with Ovii, is at

rest relative to the observer (before the redshift correction was performed), and it could be due to calibration uncertainties.

Boller et al. (2007) modeled the broad EPIC feature with only one Gaussian profile and a collisionally ionized plasma. For the line, they found a central energy of $0.554^{+0.002}_{-0.003}$ keV and a width of $0.013^{+0.004}_{-0.003}$ keV. They concluded that this line is originated in the broad line region. Even when the central energy found by Boller and collaborators is compatible – considering the errors – with our estimation, the line they found is narrower than our lines.

High-resolution spectral features

We used narrow lines (widths fixed to the instrumental resolution) to fit the narrow emission features seen in the RGS spectra of Mrk 110. To do this we introduced a second triplet and a single Gaussian to model the lines that are probably related to emission from O VII and O VIII, respectively. Again, we fixed the relative energies of the triplet lines to the laboratory values. For the O VII triplet we find energies of about 0.5669, 0.5615, and 0.5539 keV (21.9, 22.1, and 22.4 Å; unconstrained values), implying a velocity of about 3700 km s^{-1} ($z \sim 0.012$). The flux errors in the O VII lines do not allow us to obtain the coefficients that are commonly used to estimate the density and temperature of the emitting gas (Gabriel & Jordan 1969; Porquet & Dubau 2000). The O VIII line is located at a central energy of $0.652^{+0.004}_{-0.005}$ keV (~ 19 Å), which is compatible with being at the rest frame of Mrk 110. We do not find any other line significant to the fit.

Boller et al. (2007) also used narrow lines to model the narrow features. They model the same features associated with the oxygen plus two more lines from N VII-Ly α ($E_{\text{lab}} = 0.4994$ keV, i.e., $\lambda_{\text{lab}} = 24.8$ Å) and C VI Ly α ($E_{\text{lab}} = 0.3668$ keV, i.e., $\lambda_{\text{lab}} = 33.8$ Å). The line parameters given by them for the oxygen lines are compatible – within the errors – with our estimations. We find neither the N VII nor C VI lines.

ESO 359-G19 RGS data show a few emission signatures that deviate from the comprehensive five-spectra continuum fit. However, they are not statistically significant when modeled with Gaussian functions.

CTS A08.12 is studied in detail in the X-ray band here by the first time. We find one statistically significant emission line in the soft band when the comprehensive five-spectra fit is performed. This line can be identified as produced by O VII. The line found has a central energy of $0.574^{+0.003}_{-0.006}$ keV (~ 21.6 Å), which is very similar to the energy of the recombination component of the O VII triplet and has a dispersion of about 0.005 keV ($\sim 2600 \text{ km s}^{-1}$).

Only in the case of Mrk 110 and CTS A08.12 do we see a feature between 15 and 17 Å in absorption that can be associated with the Fe-L UTA (Unresolve Transition Array), which is the characteristic signature of warm absorbers (Sako et al. 2001). We tested for the presence of warm absorption related with these sources using PHASE (Krongold et al. 2003), but in neither case have we found a satisfactory result that would improve the model fitting.

7. Summary and conclusions

We analyzed all the information provided by the *XMM-Newton* satellite, including the UV range, of the four Seyfert 1 galaxies: ESO 359-G19, HE 1143-1810, CTS A08.12, and Mrk 110. Our main effort, however, focused on the comprehensive analysis of

the X-ray data that allows the characterization of the observed features in each object.

All the galaxies were found to vary on long time scales of a few years, i.e. when comparing our observations with those from other missions. Variations by factors as high as 10 or more in the soft X-ray fluxes of two of the galaxies (ESO 359-G19 and CTS A08.12) were detected, with the *XMM-Newton* observations occurring in the low state. For HE 1143-1810 and Mrk 110, factors of only about 2.5 and 2, respectively, are measured for the amplitudes of the variations. This probably means that they were still in a high-luminosity state when observed by *XMM-Newton*, so they are significantly brighter than the other two (by about an order of magnitude). The detected amplitude of the variations in the hard X-rays are lower or none, sometimes owing to lack of data in the highest soft X-ray state. In the UV, we compared the OM fluxes with previous UV values from the IUE satellite, when available. The variability amplitude is low, with factors of about 2.

On short time scales, we detected correlated soft and hard X-ray variability in HE 1143-1810 and Mrk 110, those galaxies with the highest signal-to-noise ratio data, with Mrk 110 showing a 1000 s delay between the soft and hard X-rays.

The continuum of the four AGN studied can be fully characterized by a single power law in the hard X-ray range, i.e. from 2 to 10 keV, as in most other Seyfert 1 galaxies and type 1 QSO. For all four galaxies, an extra component is needed in the soft X-rays, often called the soft-X-ray excess, and found as well in the great majority of QSOs. This soft excess is successfully modeled with a black body in two of our galaxies (ESO 359-G19 and CTS A08.12) and with a steep power law in the other two (HE 1143-1810 and Mrk 110). The parameters that define all the continuum components have standard values, although in the two brightest objects the index of the hard power law continuum lies at the lower end of its distribution, with values $\Gamma = 1.2$ – 1.4 . The soft excess black body temperatures, $kT_{\text{BB}} \sim 80$ – 130 eV, are well within the ranges found in other Seyfert 1 and QSO, and so are the spectral indices of the two soft power laws.

The above standard models and parameters seem to indicate that the standard explanation for the continuous X-ray emission is valid for these galaxies: the soft photons originating in the accretion disk are Compton up-scattered by hot electrons with a thermal distribution, probably located in a corona above the accretion disk that would be responsible for the power-law hard X-ray component of the spectrum. The origin of the soft X-ray emission, as already argued by several authors, is more difficult to understand, since the maximum temperature from an accretion disk is expected to be below the above values.

No intrinsic absorption by cold material is required to explain the observations in either of our galaxies. Interestingly, none of these objects shows clear signs of partially ionized (warm) material in the vicinity of the central black hole and in the line of sight. Considering what was found for UGC 11763, the fifth object of our study, which was analysed in a previous paper (Cardaci et al. 2009), it is interesting to note that the ionized material was detected in this galaxy, which was one of the two weakest objects. This means that the lack of detection in the other galaxies is due to intrinsically weaker or absent absorption in the line of sight and not to a lower signal-to-noise ratio in the data. This is apparently at odds with the expectation that about half of the Seyfert 1 galaxies should show evidence of this warm absorption. Nonetheless, given the low number of galaxies studied, our results are fully compatible with this expectation. This is even truer if we consider that two more spectra (CTS A08.12

and Mrk 110) show hints of weak absorption, although not significant ones.

With the exception of the well-known Fe-K α line at 6.4 keV, detected in all the four objects, not many emission features have been detected in spite of our detailed analysis of RGS data of a reasonably quality. The detected iron K α lines are generally weak, sometimes even only marginally detected, and with equivalent widths as low as 50 and 70 eV in the two brightest galaxies, Mrk 110 and HE 1143-1810, respectively. The Fe-K α lines are not significantly broader than the EPIC spectral resolution. Fexxvi at 6.97 keV is detected in one of the galaxies (ESO 359-G19). The Ovii-He α triplet in the soft X-rays is detected with instrumental RGS resolution in two of the four galaxies (CTS A08.12 and Mrk 110), although not all the triplet components are always found. It is detected as a broad line in two of the galaxies, the two brightest, and, finally the Oviii-Ly α emission is detected in only one of the galaxies, Mrk 110.

If they could be extrapolated to the Seyfert 1 galaxies as a class, the above results would mean that only a few and very weak emission features can be expected in their X-ray spectra. This is in line with what has been reported in the literature. That we detected several of our galaxies in a low state means that the absence of clear emission lines cannot be fully attributed to dilution of those lines by a strong continuum.

Acknowledgements. This research is completely based on observations obtained with *XMM-Newton*, an ESA science mission with instruments and contributions directly funded by ESA Member States and NASA. For the spectral fitting, software provided by the Chandra X-ray Centre (CXC) in the application package Sherpa was used.

This work has been supported by DGICYT grant AYA2007-67965-C03-03. MC acknowledge support from the Spanish MEC through FPU grant AP2004-0977. Furthermore, partial support from the Comunidad de Madrid under grants S-0505/ESP/000237 (ASTROCAM) and S-0505/ESP-0361 (ASTRID) is acknowledged. M.C. and G.H. also acknowledge the hospitality of the UNAM. Y.K. acknowledges support from the Faculty of the European Space Astronomy Centre (ESAC) and the hospitality of ESAC.

References

- Bauer, F. E., Condon, J. J., Thuan, T. X., & Broderick, J. J. 2000, *ApJS*, 129, 547
 Bianchi, S., La Franca, F., Matt, G., et al. 2008, *MNRAS*, 389, L52
 Bischoff, K., & Kollatschny, W. 1999, *A&A*, 345, 49
 Boller, T., Balestra, I., & Kollatschny, W. 2007, *A&A*, 465, 87
 Boroson, T. A., & Green, R. F. 1992, *ApJS*, 80, 109
 Cardaci, M. V., Santos-Lleo, M., Krongold, Y., et al. 2009, *A&A*, 505, 541
 da Costa, L. N., Willmer, C. N. A., Pellegrini, P. S., et al. 1998, *AJ*, 116, 1
 Dasgupta, S., & Rao, A. R. 2006, *ApJ*, 651, L13
 de Marco, B., Iwasawa, K., Cappi, M., et al. 2009, *A&A*, 507, 159
 den Herder, J. W., Brinkman, A. C., Kahn, S. M., et al. 2001, *A&A*, 365, L7
 Dickey, J. M., & Lockman, F. J. 1990, *ARA&A*, 28, 215
 Dunn, J. P., Crenshaw, D. M., Kraemer, S. B., & Gabel, J. R. 2007, *AJ*, 134, 1061
 Ebisawa, K., Bourban, G., Bodaghee, A., Mowlavi, N., & Courvoisier, T. 2003, *A&A*, 411, L59
 Elvis, M., Plummer, D., Schachter, J., & Fabbiano, G. 1992, *ApJS*, 80, 257
 Fairall, A. P. 1988, *MNRAS*, 233, 691
 Ford, E., Kaaret, P., Tavani, M., et al. 1996, *ApJ*, 469, L37
 Freeman, P., Doe, S., & Siemiginowska, A. 2001, in *SPIE Conf. 4477*, ed. J.-L. Starck, & F. D. Murtagh, 76
 Fuhrmeister, B., & Schmitt, J. H. M. M. 2003, *A&A*, 403, 247
 Gabriel, A. H., & Jordan, C. 1969, *MNRAS*, 145, 241
 Gehrels, N. 1986, *ApJ*, 303, 336
 Grupe, D., Thomas, H. C., & Beuermann, K. 2001, *A&A*, 367, 470
 Grupe, D., Wills, B. J., Leighly, K. M., & Meusinger, H. 2004, *AJ*, 127, 156
 Grupe, D., Komossa, S., Leighly, K. M., & Page, K. L. 2010, *ApJS*, 187, 64
 Hutchings, J. B., & Craven, S. E. 1988, *AJ*, 95, 677
 Jahnke, K., & Wisotzki, L. 2003, *MNRAS*, 346, 304
 Jansen, F., Lumb, D., Altieri, B., et al. 2001, *A&A*, 365, L1
 Karachentsev, I. D., & Makarov, D. A. 1996, *AJ*, 111, 794
 Krolik, J. H. 1999, *Active galactic nuclei: from the central black hole to the galactic environment* (Princeton, New Jersey: Princeton University Press)
 Krongold, Y., Nicastro, F., Brickhouse, N. S., et al. 2003, *ApJ*, 597, 832
 Longinotti, A. L., Bianchi, S., Santos-Lleo, M., et al. 2007, *A&A*, 470, 73
 Mason, K. O., Breeveld, A., Much, R., et al. 2001, *A&A*, 365, L36
 Mauch, T., & Sadler, E. M. 2007, *MNRAS*, 375, 931
 Maza, J., Ruiz, M. T., Gonzalez, L. E., & Wischnjewsky, M. 1992, *Rev. Mex. Astron. Astrofis.*, 24, 147
 Maza, J., Ruiz, M. T., Gonzalez, L. E., Wischnjewsky, M., & Antezana, R. 1994, *Rev. Mex. Astron. Astrofis.*, 28, 187
 Nandra, K., & Pounds, K. A. 1994, *MNRAS*, 268, 405
 Nandra, K., O'Neill, P. M., George, I. M., & Reeves, J. N. 2007, *MNRAS*, 382, 194
 Peterson, B. M. 1997, *An Introduction to Active Galactic Nuclei* (Cambridge, New York: Cambridge University Press), ISBN 0521473489
 Piconcelli, E., Jimenez-Bailón, E., Guainazzi, M., et al. 2004, *MNRAS*, 351, 161
 Piconcelli, E., Jimenez-Bailón, E., Guainazzi, M., et al. 2005, *A&A*, 432, 15
 Porquet, D., & Dubau, J. 2000, *A&AS*, 143, 495
 Protassov, R., van Dyk, D. A., Connors, A., Kashyap, V. L., & Siemiginowska, A. 2002, *ApJ*, 571, 545
 Reeves, J. N., & Turner, M. J. L. 2000, *MNRAS*, 316, 234
 Reimers, D., Koehler, T., & Wisotzki, L. 1996, *A&AS*, 115, 235
 Remillard, R. A., Bradt, H. V., Buckley, D. A. H., et al. 1986, *ApJ*, 301, 742
 Reynolds, C. S. 1997, *MNRAS*, 286, 513
 Rodríguez-Ardila, A., Pastoriza, M. G., & Donzelli, C. J. 2000, *ApJS*, 126, 63
 Sako, M., Kahn, S. M., Behar, E., et al. 2001, *A&A*, 365, L168
 Silva, D. R., & Doxsey, R. E. 2006, *Observatory Operations: Strategies, Processes, and Systems*, *SPIE Conf. Ser.*, 6270
 Simcoe, R., McLeod, K. K., Schachter, J., & Elvis, M. 1997, *ApJ*, 489, 615
 Sunyaev, R. A., & Titarchuk, L. G. 1980, *A&A*, 86, 121
 Thomas, H.-C., Beuermann, K., Reinsch, K., et al. 1998, *A&A*, 335, 467
 Turner, M. J. L., Abbey, A., Arnaud, M., et al. 2001, *A&A*, 365, L27
 Vasudevan, R. V., & Fabian, A. C. 2009, *MNRAS*, 392, 1124
 Véron-Cetty, M.-P., & Véron, P. 2006, *A&A*, 455, 773
 Verrecchia, F., in't Zand, J. J. M., Giommi, P., et al. 2007, *A&A*, 472, 705
 Voges, W., Aschenbach, B., Boller, T., et al. 1999, *A&A*, 349, 389
 Wakker, B. P., Savage, B. D., Sembach, K. R., et al. 2003, *ApJS*, 146, 1
 Wilkes, B. J., & Elvis, M. 1987, *ApJ*, 323, 243
 Winter, L. M., Mushotzky, R. F., Reynolds, C. S., & Tueller, J. 2009, *ApJ*, 690, 1322
 Wisotzki, L., Koehler, T., Groot, D., & Reimers, D. 1996, *A&AS*, 115, 227
 XMM-Newton SAS Users Guide 2004, *User's Guide to the XMM-Newton Science Analysis System (Issue 3.1)*, Based on contributions from M. Ehle, A. Pollock, A. Talavera, C. Gabriel, B. Chen, J. Ballet, K. Dennerl, M. Freyberg, M. Guainazzi, M. Kirsch, L. Metcalfe, J. Osborne, W. Pietsch, R. Saxton, M. Smith, & E. Verdugo
 XMM-Newton Users Handbook 2010, Issue 2.8.1 (ESA: XMM-Newton SOC)